



TiO₂/graphene composite photocatalysts for NO_x removal: A comparison of surfactant-stabilized graphene and reduced graphene oxide

A. Trapalis^{a,b}, N. Todorova^{a,*}, T. Giannakopoulou^a, N. Boukos^a, T. Speliotis^a,
D. Dimotikali^b, Jianguo Yu^c

^a Institute for Nanoscience and Nanotechnology, NCSR Demokritos, 15310 Agia Paraskevi, Attikis, Greece

^b School of Chemical Engineering, National Technical University of Athens, 15780 Athens, Greece

^c State Key Laboratory of Advanced Technology for Materials Synthesis and Proceeding, Wuhan University of Technology, 430070 Wuhan, China

ARTICLE INFO

Article history:

Received 9 March 2015

Received in revised form 22 June 2015

Accepted 7 July 2015

Available online 15 July 2015

Keywords:

Graphene

Reduced graphene oxide

Titanium dioxide

Photocatalysis

NO_x removal

ABSTRACT

Nanocomposite TiO₂/graphene photocatalysts were synthesized via solvothermal process using titanium isopropoxide as a TiO₂ precursor. Surfactant-stabilized graphene (ssG) prepared via liquid phase exfoliation and graphene oxide (GO) obtained via oxidation of graphite were used for preparation of two types of composites TiO₂/G and TiO₂/rGO, respectively, each with graphene loadings 0.01%, 0.1% and 1%. Hydrophilic non ionic surfactant Pluronic F127 was employed in order graphene stabilization in water and homogeneous dispersion with the TiO₂ precursor to be achieved.

The crystalline structure, composition, morphology, porosity and light absorption of the photocatalysts and their photocatalytic activity in NO_x oxidation under UV and visible light irradiation were comparatively investigated. The titania/graphene (ssG and rGO) nanocomposites exhibited higher photocatalytic efficiency than pure TiO₂ especially under visible light irradiation in terms of total NO_x (NO and NO₂) removal and NO₂ emission. Differences in the photocatalytic efficiency between the TiO₂/G and TiO₂/rGO composites were observed originating from the type and the loading of the graphene. In general, the TiO₂/rGO exhibited superior efficiency than the TiO₂/G and the best results were recorded for low 0.1% graphene loading. The findings are discussed taking into consideration the variation in the BET SSA and the E_g values, as well as the differences in the electronic structure of the ssG and the rGO, the former to be a zero-band gap material and the latter a semiconductor with tunable band gap. The presence of graphene component was determined as a key parameter governing the separation of the photogenerated electron–holes pair through interfacial charge transfer. The significantly increased activity of the TiO₂/rGO composites under visible light in NO_x removal and the very low levels of NO₂ release in comparison to the pure TiO₂ render these materials promising photocatalysts for efficient air purification.

© 2015 Elsevier B.V. All rights reserved.

1. Introduction

Air purification has attracted a lot of interest as air pollution has been linked to various health problems such as premature deaths and respiratory diseases, especially in large industrial centers [1,2]. Nitrogen oxides known as NO_x are among the pollutants whose concentration is monitored due to their negative effect on human health and their participation in the formation of smog and acid rain [3]. Nitrogen oxides are formed at high temperatures through an endothermic reaction between nitrogen and oxygen in the gas

phase [4]. Currently, NO and NO₂ are commonly emitted from combustion processes that take place in internal combustion engines [5]. Therefore, development of a method for efficient removal of nitrogen oxides from the atmosphere is of great importance for the preservation of air quality.

One way to approach this issue is using photocatalysis. Since the discovery of the photocatalytic properties of semiconductors by Fujishima and Honda in 1972 [6], a lot of research has been devoted to understanding the fundamental mechanisms involved in the photocatalytic activity of TiO₂ and other semiconductors [7–9]. The mechanism is mainly explained by the semiconductors' ability to create electron–hole pairs under illumination followed by the generation of free radicals able to undergo secondary reactions [8]. The reactions of these radicals with liquid or gas phase

* Corresponding author. Fax: +30 2106519430.

E-mail address: n.todorova@inn.demikritos.gr (N. Todorova).

pollutants cause their degradation through oxidation or reduction processes [9]. The energy required to produce electron–hole pairs in a semiconductor depends on its energy band gap. The band gap of anatase TiO_2 ~ 3.2 eV [10] enables titania to be photocatalytically active under UV irradiation. In order to improve the efficiency of the photocatalytic process, several approaches have been proposed [11]. These can be summed up as follows: (a) narrowing the effective band gap of the photocatalyst, (b) reducing the recombination rate of electron–hole pairs and (c) improving the adsorption ability of the photocatalyst, all of them being very important factors in heterogeneous catalysis.

Since the discovery of graphene in 2004 [12], this 2D material with exciting properties has been investigated for a variety of possible applications. Graphene has been investigated for preparation of composites with various semiconductors like TiO_2 [13], ZnO [14], CdS [15] aiming at enhanced photocatalytic activity. Graphene makes a compelling case due to its excellent electron-transport property and 2D geometry [16,17]. The widely recognized role of graphene as photoelectron reservoir is connected with its high conductivity. The photogenerated electrons can be more successfully accepted, stored and shuttled away from the TiO_2 /graphene interface when using graphene with low defects content, ideally defect-free pure graphene sheets. The role of the interfacial contact between graphene sheets and semiconductor nanoparticles is also considered essential for the effective transfer of photoinduced electrons [18,19]. The decreased electron–hole recombination and extended lifetime resulting from their separation is proposed as the key factor for improving the photocatalytic performance of TiO_2 /graphene nanocomposites [16,20].

Different types of graphene can be obtained depending on the preparation routes. Thus, pure graphene is prepared by exfoliation of graphite in some organic solvents or in water, provided that it is properly modified or with the addition of surfactants that stabilize graphene layers in a dispersion [21]. Graphene is also prepared via oxidation of graphite to graphite oxide (GtO) and further treatment to reduced graphene oxide (rGO). This route is highly preferred due to the presence of covalently bonded oxygen functionalities on the GtO sheets that facilitate the processing of this intermediate and the synthesis of various composites including TiO_2 /graphene photocatalysts. Although the rGO is widely used as a substitute for graphene, it has more structural defects than non-modified graphene which impact its electrical properties [22]. Specifically, the electronic conductivity of rGO that depends on the level of its reduction is lower than the conductivity of the ideal single-layer, defect-free, non-oxygenated graphene which could lead to decreased e^- transfer and e^- – h^+ separation [16,23,24]. Therefore, how different types of graphene perform when used for the same application such as TiO_2 -based photocatalysis is worth of investigation.

A variety of different synthesis strategies have been employed for the preparation of TiO_2 /graphene composites. The vast majority of the publications are dedicated to preparation and investigation of composites using reduced graphene oxide as graphene component [25–39]. The photocatalytic efficiency of these composites has been evaluated for the degradation of several pollutants with overall promising results. Specifically, TiO_2 /graphene oxide composites have been studied for the degradation of methyl orange [25,26], methylene blue [27,28] and hydrogen evolution [29]. The observed enhanced photocatalytic performance was attributed to an increased adsorption capacity of these photocatalysts [26]. It was also proposed that graphene oxide acts as a photosensitizer, increasing the activity of the photocatalyst under visible light [14,16,27]. TiO_2 /rGO composites in which the graphene oxide component has been reduced by thermal, solvothermal or photochemical treatment have been investigated for degradation of phenol [30], rhodamine B [31,32], aldicarb and norfloxacin [31], methylene blue [33–35], methyl orange [38], malachite green

[37], 2,4-dichlorophenoxyacetic acid [38], water disinfection from *Escherichia coli* and *Fusarium solani* spores [39], hydrogen evolution [40], etc. The majority of these studies attribute the enhanced photocatalytic performance of the TiO_2 /graphene composites in comparison to bare TiO_2 to a more efficient charge carrier separation due to an interfacial electron transfer to the graphene sheets.

To this point, coupling of TiO_2 with pure graphene sheets with low defect density is a great challenge due the lack of hydrophilic functional groups on the graphene sheets that could be utilized for their homogeneous dispersion and bonding with the hydrophilic TiO_2 [41]. The photocatalytic performance of such composites for environmental applications is poorly investigated in comparison to TiO_2 /rGO photocatalysts. Photoreduction of 4-nitrophenol pollutant in aqueous solution under visible light has been reported by graphene nanoplatelets (GNP)-encapsulated TiO_2 . The composites were prepared via electron spinning with the GNPs to be initially functionalized with $-\text{COOH}$ groups [42]. Graphene exfoliated in *N,N*-dimethyl-formamide (DMF) solvent has been modified with ethyl cellulose and terpineol prior coupling with commercial titania P25. The moderate enhancement in acetaldehyde oxidation and significant enhancement in CO_2 reduction under solar light was attributed to superior electrical mobility which facilitates the diffusion of the photoexcited electrons to reactive sites [43]. Also, TiO_2 has been in situ synthesized from water soluble TiF_4 precursor using graphene nanosheets exfoliated in DMF solvent as 2D platform and polyvinylpyrrolidone as graphene-titania mediator. The combined strategy of decreasing the defects density and increasing the interfacial contact yielded in enhanced oxidation of alcohols to aldehydes [18]. To the best of our knowledge, there is no experimental data on preparation of TiO_2 /pure graphene photocatalysts via water-dispersed graphene favoring the homogeneous crystallization of the TiO_2 onto the 2D surface.

In the present work, TiO_2 semiconductor was coupled with two types of graphene: (a) surfactant-stabilized graphene prepared by exfoliation of graphite and (b) reduced graphene oxide prepared via oxidation of graphite. TiO_2 /graphene composites with different graphene content were synthesized and comparatively investigated with emphasis on their efficiency in photocatalytic removal of NO_x pollutants from ambient air. To our comprehension, this is the first time these photocatalysts have been studied in this context.

2. Experimental

The TiO_2 /graphene nanocomposites were prepared in two stages. First, aqueous dispersions of surfactant-stabilized graphene (ssG) and graphene oxide (GO) were prepared by strong sonication of natural graphite and graphite oxide, respectively. Then, TiO_2 was synthesized in presence of graphene/graphene oxide applying solvothermal treatment where the GO was reduced to rGO.

2.1. Preparation of surfactant-stabilized graphene

Dispersions of ssG were prepared adopting the procedure described in [44]. Specifically, 1 g of natural graphite (100 mesh, Alfa Aesar) was mixed with 500 mg of Pluronic F127 (Sigma–Aldrich) in 100 mL of deionized (DI) water. The mixture was stirred for 10 min, placed in an ice bath and transferred to a probe sonicator (Hielscher Ultrasound Technology UIP1000hd) where it was sonicated for 2 h at 50% amplitude. The prepared dispersions were centrifuged at 4000 RPM for 10 min in order to precipitate larger graphene flakes and non-exfoliated graphite. Finally, the supernatant was carefully collected and stored. The resulting dispersions were black in color and remained stable for several weeks.

2.2. Preparation of graphene oxide dispersions

Graphite oxide was prepared from natural graphite applying a modified Hummers method [45]. Briefly, 2 g of natural graphite (100 mesh, Alfa Aesar) and 1 g of NaNO₃ (Sigma-Aldrich) were mixed with 80 mL of concentrated H₂SO₄ (97%, Riedel de Haen) under stirring in an ice bath to prevent overheating. Six grams of KMnO₄ (Sigma-Aldrich) were slowly added to the mixture while keeping the temperature at around 10 °C. After the addition of KMnO₄, the solution was removed from the ice bath and kept at 35 °C for 90 min under strong stirring. 100 mL of DI H₂O were added dropwise causing a rise in temperature. The solution was kept at 95 °C for 15 min. Then, 90 mL of 3% H₂O₂ (Sigma-Aldrich) were added. Finally, the solution was diluted by adding a large amount of DI water. After leaving the solution to rest for 24 h, the supernatant was removed and the precipitant was washed repeatedly with DI water, dried and collected in the form of paper-like sheets.

In order to prepare aqueous dispersions of graphene oxide, 100 mg of graphite oxide were sonicated in 100 mL of DI H₂O in a sonication bath for 1 h. The resulting dispersions were brown in color and remained stable for weeks. To assess the degree of reduction of GO during the consequent solvothermal synthesis of TiO₂, 30 mL GO dispersion was transferred to autoclave and heated at 180 °C for 2 h. The target temperature was reached with the autoclave in the oven and the sample was collected after cooling naturally to room temperature. The color of the obtained solution changed to black and the resulting solid material was labeled rGO.

2.3. Preparation of nanocrystalline TiO₂ and TiO₂/graphene nanocomposites

Initially, a TiO₂ sample was prepared according to the procedure given in [46], which provides nanocrystalline anatase TiO₂ powder. Specifically, 1 g of the Pluronic F127 block copolymer (Sigma-Aldrich) was mixed with 113 mL of ethanol and 1 mL of 1 M HNO₃. The mixture was stirred for 10 min and 7 g of the TiO₂ precursor Ti(OC₃H₇)₄ (Merck) were added dropwise. The solution was transferred to autoclaves and heated at 180 °C for 2 h. After cooling to room temperature, the precipitate was washed with DI water, dried, ground and the collected powder was labeled TiO₂-F. It should be noted that Pluronic F127 was added to provide a common frame of reference for all samples, considering that the ssG used for the preparation of the composites was stabilized with the same surfactant. Also, for comparison reasons titania sample without Pluronic F127 block copolymer was prepared using the same procedure, which was labeled TiO₂.

For the synthesis of the TiO₂/graphene composite materials, an appropriate amount of ssG or GO dispersion was added to the TiO₂ precursor mixture and solvothermally treated as described above. TiO₂/ssG and TiO₂/rGO composites with addition of 0.01 w/w%, 0.1 w/w% and 1 w/w% of ssG and GO, respectively, were prepared. The powders obtained were labeled TiO₂/G-1, TiO₂/G-2, TiO₂/G-3 and TiO₂/rGO-1, TiO₂/rGO-2, TiO₂/rGO-3, correspondingly. The nomination of all the prepared materials is given in Table 1.

2.4. Characterization

X-ray diffraction (XRD) patterns were obtained on a Siemens D500 diffractometer with secondary graphite monochromator and CuKα radiation in Bragg–Bretano geometry. The measured 2θ range between 10° and 90° was scanned with the velocity of 0.03°/2 s. Scanning Electron Microscopy (SEM) images were recorded with a FEI Inspect Microscope equipped with tungsten filament operating at 25 kV and secondary detector for image formation. Transmission electron microscopy (TEM) analysis was conducted with a FEI CM20 microscope using 200 kV accelerating voltage. TEM specimens were

prepared by drop casting 2 μL of TiO₂/graphene–ethanol suspension on holey carbon Cu TEM grids. N₂ adsorption/desorption measurements were carried out using a Micromeritics ASAP 2020 apparatus. All the samples were degassed at 180 °C prior to nitrogen adsorption measurements. UV–vis absorption and diffuse reflectance spectra were obtained using a UV–vis spectrophotometer UV-2100 Shimadzu. Fourier Transform Infrared spectra (FT-IR) were acquired using a Bruker Equinox 55/SFTIR spectrometer. Raman spectra were obtained on a Renishaw inVia Raman Microscope spectrophotometer with a 514.5 nm Ar⁺ laser.

2.5. Photocatalytic activity

The photocatalytic activity of the prepared materials was evaluated for the removal of nitrogen oxides applying standard ISO/DIS-22197-1 procedure [47]. The powders were pressed in holders with surface area 19.6 cm² and irradiated with UV-A light (~10 W/m²) for 16 h before measurements in order to remove any residual organic contaminants from the surface of the photocatalysts. The photocatalytic activity was evaluated under UV-A and visible light irradiation. Philips Cleo Compact 15 W lamps were used as a UV-A light source and 4 Nordex T5 8 W 4000K lamps were used as a source of visible light. The irradiation intensities on the sample level were ~10 W/m² and ~7000 lux for the UV-A and the visible light, respectively.

The samples were placed in flow-type photoreactor where model air containing 1 ppm NO and humidity ~50% was supplied through a flow-controlling system with a rate 3 L/min. The NO gas pollutant was supplied from a gas container with 50 ppm NO concentration in N₂ (Linde Hellas). The relative humidity of ~50% was obtained using mixture of dry and wet air. The concentrations of NO and NO₂ in the air above the samples were monitored by an ambient NOx analyzer APNA-370HORIBA using cross-flow modulated semi decomposition chemiluminescence method and recorded in 5 s intervals. Before irradiation, the samples were kept in dark for 5 min in order to achieve saturation of the photocatalysts and thus avoid error in decrease of NO due to initial adsorption phenomenon. The duration of the illumination period was 30 min.

The efficiency of the photocatalysts in NO oxidation (γ_{NO}), NO₂ formation (γ_{NO2}) and NOx removal (γ_{NOx}) was assessed using the Eqs. (1)–(3):

$$\gamma_{\text{NO}} = \frac{\int_{t_0}^{t_1} (\text{NO}_{\text{in}} - \text{NO}_{\text{meas}}) dt}{\text{NO}_{\text{in}} T} \times 100 \quad (1)$$

$$\gamma_{\text{NO}_2} = \frac{\int_{t_0}^{t_1} (\text{NO}_{2\text{meas}} - \text{NO}_{2\text{in}}) dt}{\text{NO}_{\text{in}} T} \times 100 \quad (2)$$

$$\gamma_{\text{NO}_x} = \frac{\int_{t_0}^{t_1} (\text{NO}_{x\text{in}} - \text{NO}_{x\text{meas}}) dt}{\text{NO}_{x\text{in}} T} \times 100 \quad (3)$$

where NO_{in}, NO_{xin} and NO_{2in} are the initial NO, NOx and NO₂ concentrations, respectively. NO_{meas}, NO_{xmeas} and NO_{2meas} are the measured NO, NOx and NO₂ concentrations, respectively. *t*₀ and *t*₁ are the time moments when UV light was switched on and off, respectively. *T* is the duration of the illumination period determined by difference *T* = *t*₁ – *t*₀. More detailed description of the equations and the experimental conditions for the photocatalytic activity measurements can be found in [48,49].

3. Results and discussion

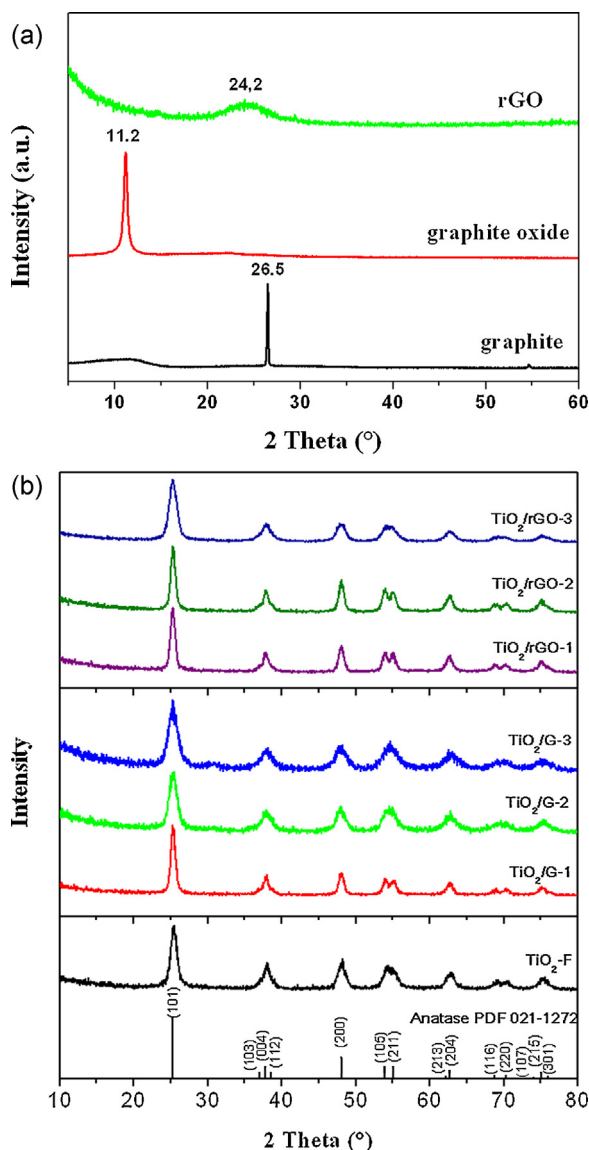
3.1. Crystalline structure

The XRD patterns of the initial natural graphite as well as the prepared graphite oxide and rGO are shown in Fig. 1a. In the pat-

Table 1

Description of the samples, crystallite size, BET specific surface area, average pore size and band gap values for the prepared photocatalysts.

Nominal name	Presence of Pluronic F127	Graphene content (w/w%)	Crystallite size (nm)	BET SSA (m ² /g)	Pore size (nm)	Band gap energy (eV)
TiO ₂	–	–	6.69	201.92	4.16	3.20
TiO ₂ -F	+	–	7.29	176.98	5.57	3.20
TiO ₂ /G-1	+	0.01	10.16	142.67	5.51	3.14
TiO ₂ /G-2	+	0.10	6.06	195.40	4.99	3.16
TiO ₂ /G-3	+	1.00	5.10	225.41	4.40	3.08
TiO ₂ /rGO-1	+	0.01	10.58	130.34	5.71	3.19
TiO ₂ /rGO-2	+	0.10	10.10	138.01	5.62	3.16
TiO ₂ /rGO-3	+	1.00	6.26	195.79	4.86	3.12

**Fig. 1.** X-ray Diffraction patterns of: (a) natural graphite, graphite oxide and rGO, (b) pure TiO₂ and composite materials TiO₂/rGO and TiO₂/G.

tern of natural graphite the characteristic (002) peak at 26.5° is evident which after the oxidation process was shifted to 11.2°. The shift of the peak in the graphite oxide is attributed to the introduction of functional groups between the graphite layers which cause an increase of the interlayer distance (d-spacing) [50,51]. The value of the d-spacing calculated using Bragg's law is 0.336 nm for the natural graphite, while for the graphite oxide it was elevated to 0.789 nm. In the pattern of the graphite oxide, reflection originating

from residual non-oxidized graphite was not present manifesting complete graphite oxidation. After the solvothermal treatment (sample rGO), a weak broad peak at 24.2° can be observed in the XRD pattern. This backward shift to higher 2θ in the rGO is attributed to the reverse process, namely the removal of functional groups from GO during the solvothermal processing. Accordingly, the d-spacing value for rGO was decreased to 0.368 nm. These results indicate the partial reduction of GO by the applied treatment. The fact that the peak of rGO is relatively broad and weak indicates a high degree of exfoliation and formation of few layer rGO sheets.

The XRD patterns of the prepared pure TiO₂ as well as of the composite TiO₂/rGO and TiO₂/G materials are shown in Fig. 1b. The peaks recorded for all materials in the 10–80° range match the diffraction pattern of TiO₂ anatase phase (PDF-021-1272) determining the crystal structure of the prepared TiO₂. The average crystallite size of the TiO₂ and TiO₂/graphene composite materials was calculated using the Scherrer equation and was found to be in the range of 5–10 nm (Table 1). It can be perceived that the addition of the block copolymer Pluronic F127 to the mixture causes a slight increase in crystallite size and does not seem to impede the crystallization process, a result which is in agreement with the results for a similar treatment in literature [46]. In the composite TiO₂/G and TiO₂/rGO materials, the crystallite size was firstly increased and then decreased with the addition of graphene content. The initial increase for TiO₂/rGO-1 and TiO₂/G-1 samples was attributed to the introduction of additional H₂O with the graphene dispersions which promotes the hydrolysis reaction of titanium isopropoxide accelerating thus the crystallization of TiO₂ [52]. The subsequent decrease in crystallite size for TiO₂/G-3 and TiO₂/rGO-3 was attributed to the enhanced incorporation of graphene sheets between the nucleation centers sufficient to delay the crystallization process. The fact that the increase of graphene content up to 1% did not lead to the appearance of new diffraction peaks in either case is ascribed to: (a) possible overlapping of the anatase (101) peak at 25.3° with low intensity graphene peak at ~26° for ssG and at ~24° for rGO; (b) formation of well-mixed and uniform TiO₂/graphene nanocomposites.

3.2. Morphology and porosity

SEM images of ssG, GtO, rGO as well as pure TiO₂, composite TiO₂/G-3 and TiO₂/rGO-3 samples are shown in Fig. 2. For the ssG sample, randomly oriented flakes can be observed revealing exfoliation of initial graphite. The images of GtO and rGO revealed a highly stacked layered structure for the former, which after ultrasonic treatment in water and solvothermal processing appeared exfoliated and folded in random shapes in the latter. In TiO₂/G and TiO₂/rGO composites, individual graphene sheets are not distinguishable on the surface of the material even at the highest graphene content. It is presumed that the graphene sheets are well embedded between TiO₂ nanoparticles. For these samples, slight orientation of the TiO₂ nanoparticles can be perceived that may be

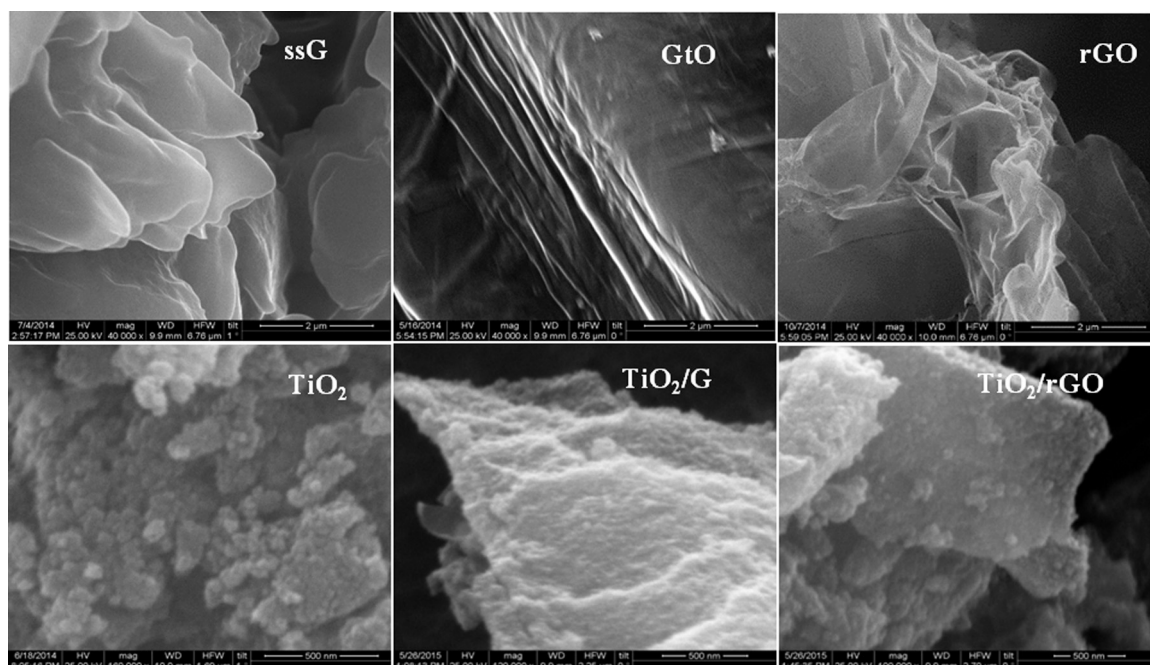


Fig. 2. Scanning electron microscopy images of the initial natural graphite, pure graphene (ssG), graphite oxide (GtO), reduced graphene oxide (rGO), TiO_2/G -3 and TiO_2/rGO -3.

linked to the structure directing feature of the incorporated layered graphene component [16,24].

The 2D graphene sheets can be clearly seen in the TEM images depicted in Fig. 3 for both types of composites TiO_2/G and TiO_2/rGO with graphene content 1%. The images show 2–6 layered graphene sheets intermixed with the TiO_2 nanoparticles. The TEM analysis also demonstrated that size of the TiO_2 crystallites is below 10 nm which is in agreement with the values estimated through XRD analysis.

The adsorption/desorption isotherms of the pure titania, TiO_2/G and TiO_2/rGO composite materials are depicted in Fig. 4. The corresponding specific surface area (SSA) values and the average pore size are listed in Table 1. It is evident that the addition of the surfactant Pluronic F127 caused a decrease in the BET SSA of the TiO_2 powder from $\sim 200 \text{ m}^2/\text{g}$ to $\sim 177 \text{ m}^2/\text{g}$ and an increase in the average pore size. The addition of 0.01% ssG and GO led to a further decrease of the BET SSA of the TiO_2/G -1 and TiO_2/rGO -1 composites down to $\sim 143 \text{ m}^2/\text{g}$ and $\sim 130 \text{ m}^2/\text{g}$, respectively. However, by increasing the weight percentage of ssG and rGO to 0.1 and 1 the SSA was gradually increased even beyond the initial value of TiO_2 -F.

Although Pluronic F127 is a surfactant often used to obtain TiO_2 with higher SSA [53], such an increase was not recorded for our sample TiO_2 -F. This outcome can be related to the method of elimination of the surfactant which is removed from the TiO_2 by combustion when high SSA is targeted. In our experiment, calcination was not applied and the surfactant was removed from the photocatalyst by washing with water. Despite its hydrophilicity and the multiple washing/centrifugation procedure, a complete removal of the surfactant can not be achieved. Therefore, it seems plausible that the interference of large Pluronic F127 molecules between TiO_2 nanoparticles is responsible for the decrease of the specific surface area. The decrease in BET SSA for TiO_2/G -1 and TiO_2/rGO -1 composites can be linked to the increased crystallite size of these materials revealed by XRD and is associated with the introduction of H_2O to the mixture. Finally, the increase in BET SSA and the decrease in the average pore size of the composites with lowering of the graphene content can be explained by the high specific surface area and porosity of ssG and rGO.

3.3. Composition and electronic structure

3.3.1. UV-vis spectroscopy

The successful exfoliation of the graphite to graphene was verified by the UV-vis absorption spectrum of the ssG dispersion shown in Fig. 5a. A strong characteristic for the graphene absorption peak at 269 nm can be observed attributed to the π - π^* electron transition in C–C bonds [44,54]. The spectrum was also employed to determine the concentration of the ssG dispersion by applying the Lambert–Beer law and using a previously determined molar absorptivity coefficient for aqueous graphene dispersions of $1390 \text{ mL mg}^{-1} \text{ m}^{-1}$ at 660 nm [55]. The concentration of graphene in the prepared ssG dispersions varied between 0.15 and 0.30 mg/mL, depending on the centrifugation speed and duration.

The UV-vis absorption spectra of the GO and rGO samples presented in Fig. 5b evidence the reduction of GO during the solvothermal treatment. The two characteristic peaks in the GO spectrum at 230 and 300 nm attributed to the π - π^* and n - π^* electron transitions in the C–C and C=O bonds, respectively [56], were altered after the solvothermal treatment. In the rGO spectrum, the broad peak at 300 nm disappeared and the absorption peak attributed to π - π^* was red shifted to 266 nm. The shift of this absorption peak was related to the restoration of electronic conjugation within the GO sheets [57,58]. The absorption peak of rGO at 266 nm correlates well with that of ssG at 269 nm indicating similar degree of conjugation in the two materials, while the disappearance of the peak at 300 nm evidenced the removal of oxygen functional groups from GO sheets.

3.3.2. FT-IR spectroscopy

The FT-IR spectra obtained for natural graphite, GO, rGO and TiO_2/rGO -3 are shown in Fig. 6. In contrast to the natural graphite, the spectrum of GO displayed several absorption peaks of oxygen functional groups, such as: carbonyl C=O stretching vibration at 1730 cm^{-1} , hydroxyl OH bending vibration from molecular water or C=C vibration in aromatic ring at 1633 cm^{-1} , C–OH bending vibration at 1400 cm^{-1} and C–OH stretching vibration at

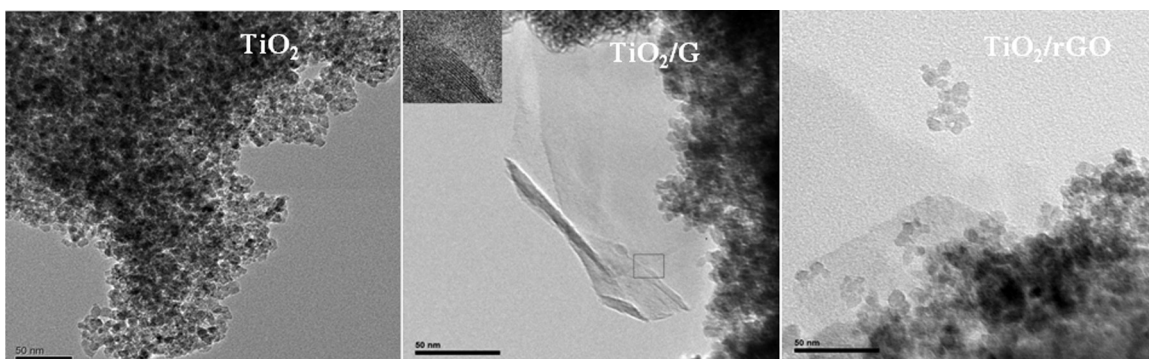


Fig. 3. TEM micrographs of: (a) pure TiO_2 and composite (b) $\text{TiO}_2/\text{G}-3$ and (c) $\text{TiO}_2/\text{rGO}-3$ materials. Inset: HRTEM image of the marked area showing the graphene sheet edge that consists of 5 layers.

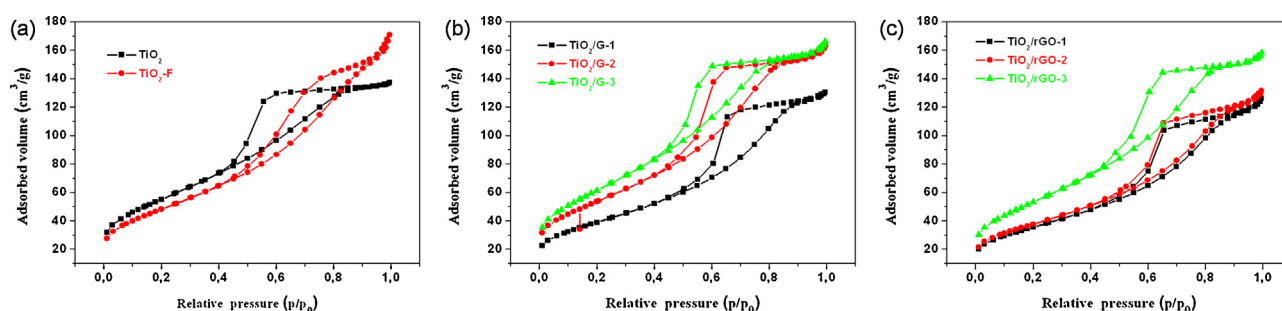


Fig. 4. Liquid N_2 adsorption–desorption isotherms for: (a) pure TiO_2 materials and composite (b) TiO_2/G and (c) TiO_2/rGO materials.

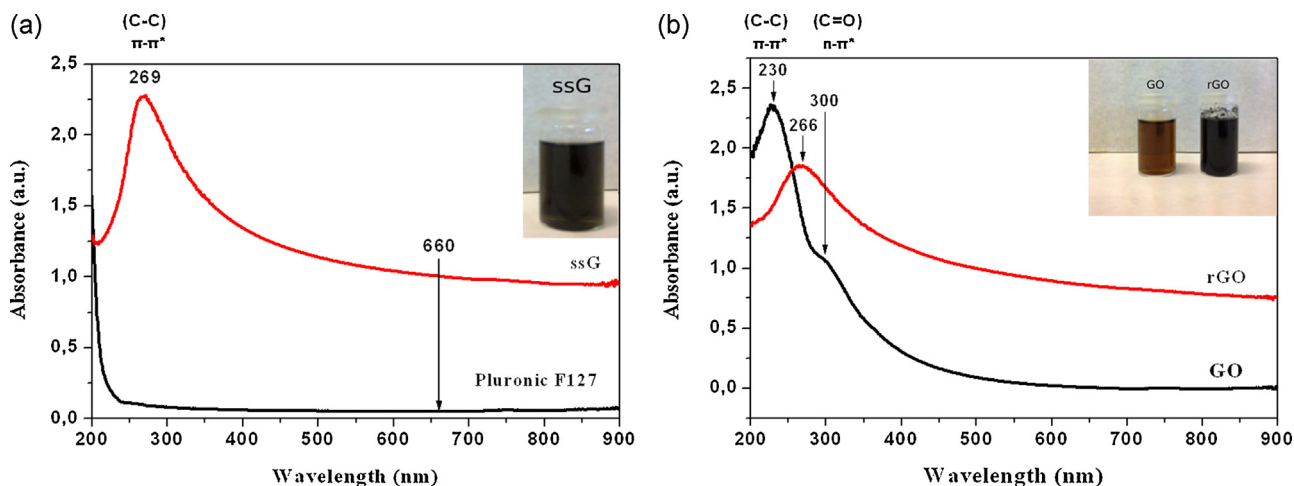


Fig. 5. UV–vis absorption spectra of: (a) ssG dispersion and Pluronic F127 aqueous solution and (b) GO and rGO dispersions. Insets: photographs of the prepared GO, ssG and rGO dispersions.

1231 cm^{-1} , as well as C–O stretching vibrations or epoxy C–O–C vibrations at 1050 cm^{-1} [30,59]. The broad peak at 3400 cm^{-1} observed in all spectra was related to the stretching vibration of hydroxyl groups of the adsorbed water [59].

After the solvothermal treatment of GO, the intensities of the C=O and C–OH peaks in the rGO spectrum decreased or disappeared. In addition, the two peaks at 1167 and 1120 cm^{-1} in the rGO spectrum related to the C–O–C stretching vibrations [60] appeared at 1167 and 1120 cm^{-1} . The formation of additional C–O–C bonds can be explained by the removal of water (H–OH) from the GO sheets. These results further indicate the reduction of GO to rGO during the solvothermal treatment and are in good accordance with the results obtained from the XRD analysis.

The spectra of the pure TiO_2 and the composite $\text{TiO}_2/\text{G}-3$ and $\text{TiO}_2/\text{rGO}-3$ exhibited a wide peak at $400\text{--}900\text{ cm}^{-1}$ which was attributed to the stretching vibration of Ti–O–Ti bonds in TiO_2 [30,61]. Peaks related to oxygen functional groups of the graphene component are not distinguishable. The spectra of the rest of the composites are not showed due to resemblance. Similarly to the SEM analysis, the transition from graphite to graphene oxide was revealed, but the presence of the graphene in the composites was not proved. This outcome was attributed to the relatively low (1%) graphene loading of TiO_2 .

3.3.3. Raman spectroscopy

The electronic structure of the components and the presence of graphene in the composite TiO_2/G and TiO_2/rGO photocatalysts were investigated using Raman spectroscopy. The measured

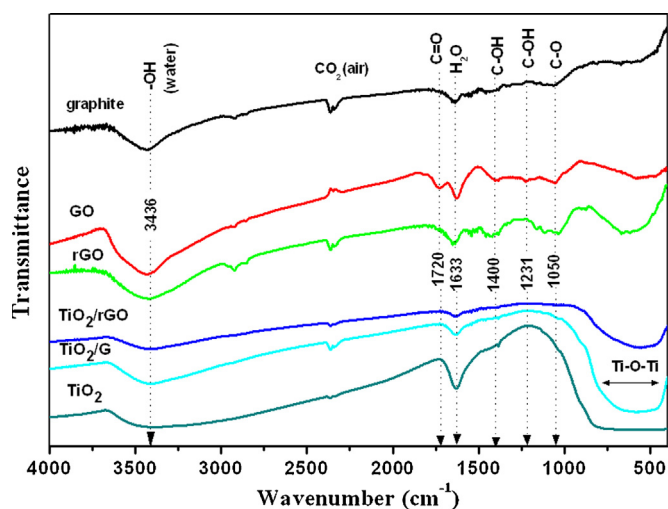


Fig. 6. FT-IR spectra of natural graphite, GO, rGO, TiO₂ and titania/graphene composites (samples TiO₂/G-3 and TiO₂/rGO-3).

Raman spectra of the initial graphite, the pure components ssG, rGO and TiO₂-F as well as the spectra of the composite materials are comparatively given in Fig. 7.

The Raman spectra of ssG and rGO (Fig. 7a) display the characteristic D, G and 2D bands of ssG and rGO correspondingly. The D band at 1350 cm⁻¹ and G band at 1600 cm⁻¹ are attributed to the edge carbons and/or disordered sp³ as well as to the ordered sp² carbon networks, correspondingly [62]. In the surfactant-stabilized graphene, the D and G bands are sharper than those in the graphene obtained by chemical oxidation due to the lower number of defects [44]. In addition, the 2D band (absent in the rGO spectrum) is well defined and more symmetrical than that of natural graphite, which indicates the formation of 1–4 layered graphene sheets [44,63]. In the rGO, the high intensity of the D band relative to the G band, as well as their broad width is associated with more structural imperfections created by the introduction of functional groups to the carbon sheets during the oxidation process [64].

The Raman spectra of the composite TiO₂/G and TiO₂/rGO materials are shown in Fig. 7b and c, respectively. The spectra display bands at 149 cm⁻¹ (E_g), 395 cm⁻¹ (B_{1g}), 517 cm⁻¹ (A_{1g}) and 640 cm⁻¹ (E_g) that originate from the TiO₂ component. The E_g bands were attributed to symmetric stretching vibrations of O–Ti–O bonds, while the B_{1g} and A_{1g} bands were related to the symmetric and asymmetric bending vibrations of O–Ti–O [65,66]. In addition to the mentioned TiO₂ modes, presence of the graphene components in the composites with the higher loading (1% ssG, 0.1% and 1% rGO) is also manifested. The graphene phase was not detected in the TiO₂/G (rGO)-1 composites due to the very low 0.01% initial loading.

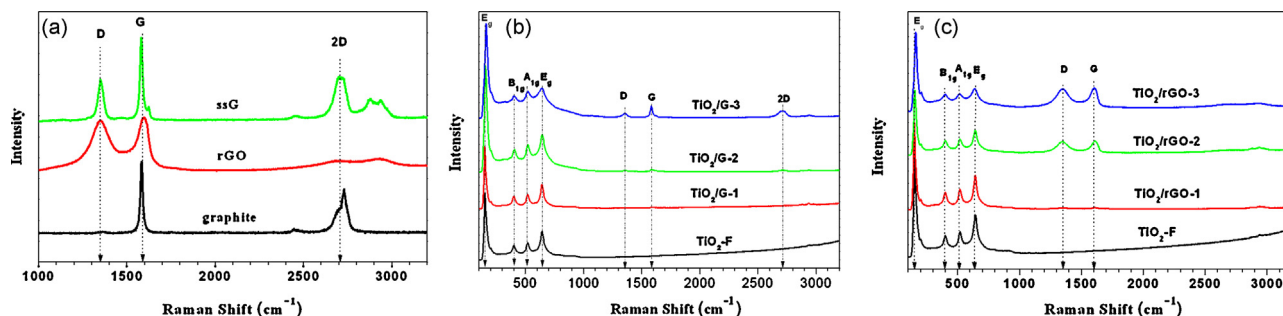


Fig. 7. Raman spectra of: (a) natural graphite, GO and ssG materials, (b) pure TiO₂ and composite TiO₂/G materials, (c) pure TiO₂ and composite TiO₂/rGO materials.

3.4. Light absorbance

Diffuse reflectance spectroscopy was used in order to estimate the effective band gap of the TiO₂, TiO₂/G and TiO₂/rGO materials. The absorption function $[f(R) \times E]^{1/2}$ was plotted against E (eV), where $f(R) = (1 - R)^2 / 2R$ is the Kubelka–Munk function expressed through the measured diffuse reflectance R of the photocatalysts [67,68] and E is the electromagnetic wave energy. The band gap was estimated at the intersection of the extrapolated linear section of the absorption function and the energy axis at zero absorption [69]. The Tauc plots received according to the extrapolation procedure are shown in Fig. 8. The diagrams revealed a small but gradual decrease in the band gap of the TiO₂/G and TiO₂/rGO composites with the increase of the graphene component content. The band gap of the composite materials decreased to 3.08 eV (TiO₂/G-3) and 3.12 eV (TiO₂/rGO-3) in comparison to the TiO₂ (3.20 eV) with and without Pluronic F127. This result can be associated with the ssG and rGO that leads to the formation of electronic states below the conductive band edge and therefore narrowing of the TiO₂ band gap [70]. Also, the composites exhibited a decrease in reflectance with the increase of graphene content in the 400–900 nm area as shown in the insets of Fig. 8. It was ascribed to the light absorbing property of graphene which was also indicated by the color change of the powder samples from light to dark gray. Notably, the TiO₂/rGO materials displayed higher absorbance in the visible region than the corresponding TiO₂/G.

3.5. Photocatalytic activity

The measurement of the photocatalytic NO_x removal from ambient air flow by the investigated materials revealed differences in their photocatalytic behavior and efficiency. It should be noted that the photocatalyst is involved in two successive oxidative reactions: (i) NO(gas) to NO₂(gas) and (ii) NO₂(gas) to NO₃⁻(solid). The variation of the concentration of the gases NO, NO₂ and NO_x(NO + NO₂) in the air above the bare TiO₂ and selected composite photocatalysts under UV and visible light irradiation are depicted in Fig. 9. In general, the graphene modified titania exhibited relatively stable photocatalytic behavior with lower NO₂ emission and higher overall NO_x removal in comparison to the pure titania.

The calculated photocatalytic efficiency values are listed in Table 2 and presented in the form of histograms in Fig. 10. Pure ssG and rGO are not included as the former being a dispersion could not be measured and the latter did not show any photocatalytic activity at the applied experimental conditions. From the data, it can be perceived that the addition of surfactant Pluronic F127 does not significantly influence the photocatalytic activity of pure TiO₂. The slightly enhanced NO_x oxidation by the TiO₂-F can be linked to the larger pore size in comparison to TiO₂ which facilitates the access of pollutants and light to the photocatalyst's surface.

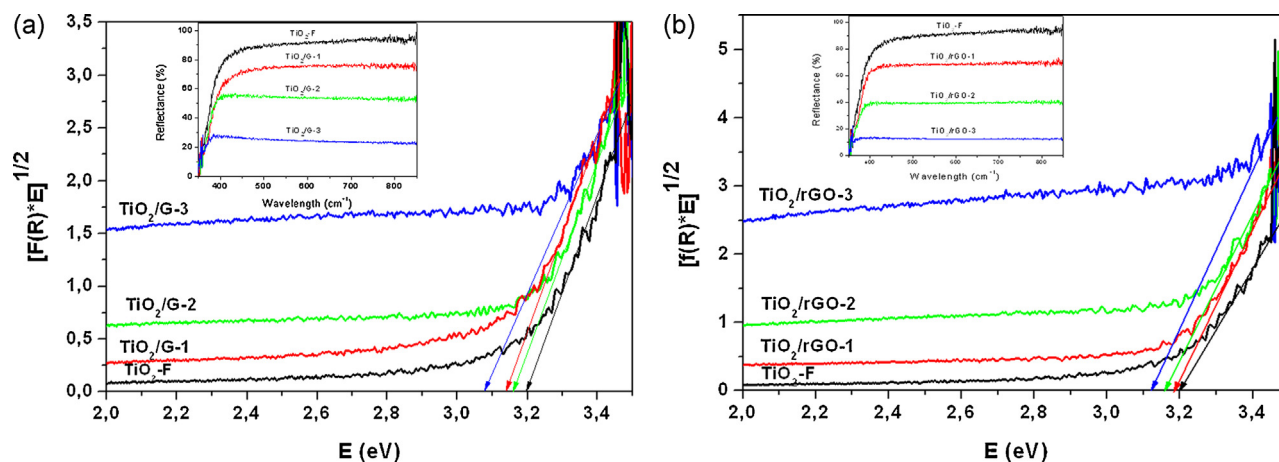


Fig. 8. Absorption function $[F(R) \times E]^{1/2}$ vs energy E for: (a) TiO_2 -F and TiO_2/G composite materials and (b) TiO_2 -F and TiO_2/rGO composite materials. Insets: measured diffuse reflectance spectra of the corresponding materials.

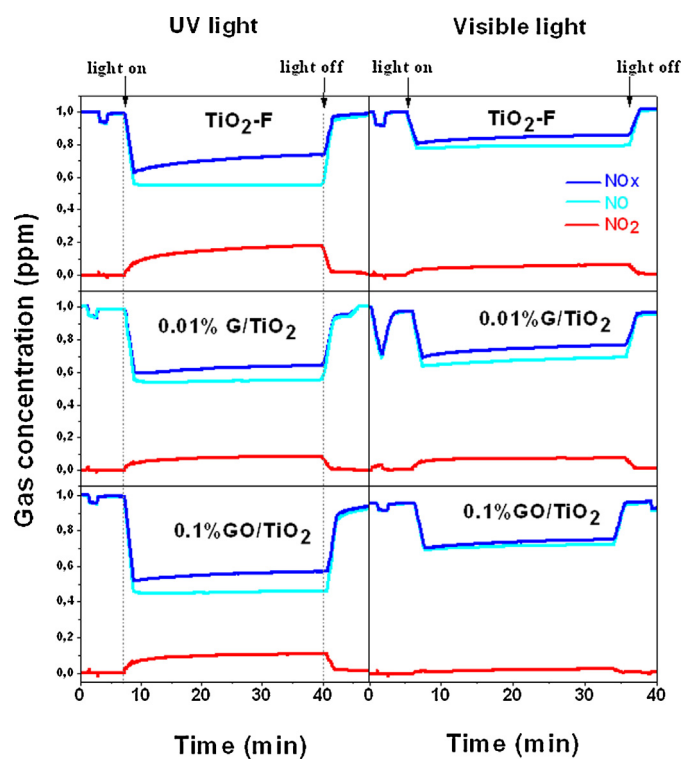


Fig. 9. Experimental concentration curves of selected pure and composite photocatalysts under UV light and visible light irradiation.

Table 2

Photocatalytic efficiency of the prepared photocatalysts in: decrease of NO, release of NO_2 and total NOx removal under UV and visible light.

Photocatalyst	UV light			Visible light		
	NO decrease (%)	NO_2 release (%)	NOx removal (%)	NO decrease (%)	NO_2 release (%)	NOx removal (%)
TiO_2	40.51	15.06	25.45	12.68	3.33	9.35
TiO_2 -F	42.57	14.37	28.20	20.34	5.13	15.20
TiO_2/G -1	42.68	7.28	35.40	29.34	6.59	22.75
TiO_2/G -2	40.00	13.74	26.26	21.46	4.87	16.59
TiO_2/G -3	42.27	12.78	29.49	13.02	0.86	12.16
TiO_2/rGO -1	47.33	7.95	39.38	25.19	4.44	20.76
TiO_2/rGO -2	52.28	9.42	42.86	24.05	1.71	22.34
TiO_2/rGO -3	47.40	5.88	41.51	20.57	0.68	19.88

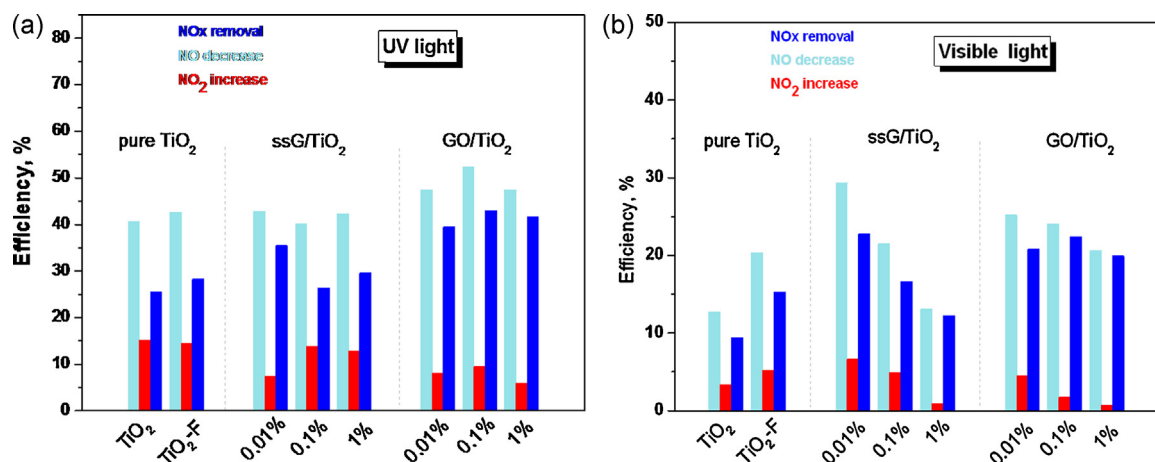


Fig. 10. Photocatalytic efficiency of pure titania compared with composite TiO₂/G and TiO₂/rGO (1–3) photocatalysts in decrease of NO, release of NO₂ and total NOx removal under: (a) UV light and (b) visible light.

Under UV light, the efficiencies of the ssG modified photocatalysts (TiO₂/G 1–3 samples) appeared similar to the reference TiO₂-F sample. In this group, the composite with the lowest graphene loading (TiO₂/G-1) exhibited the best total NOx removal and the lowest emission of the intermediate NO₂ product. The graphene oxide modified photocatalysts (TiO₂/rGO 1–3 samples) demonstrated a slight increase in photocatalytic efficiency. The TiO₂/rGO-2 exhibited the highest efficiency in both NO decrease (~52%) and NOx removal (~43%), the corresponding values for the TiO₂-F being ~42% and ~28%.

Under visible light, it can be observed that the addition of ssG and rGO led to a significant enhancement of NO oxidation along with preserving remarkably low levels of NO₂ emission. Notably, the efficiency in NO oxidation is gradually elevated with the decrease of the graphene (ssG or rGO) loading. The TiO₂/G-1 and TiO₂/rGO-2 photocatalysts exhibited the lowest NO₂ release in the air and the highest efficiency for NOx removal. The increased activity of the composites is accredited to the influence of the graphene component but not to favorable specific surface area or width of the band gap, as the materials with the highest efficiency are those (TiO₂/G-1 and TiO₂/rGO-2) with relatively low SSA (~143 m²/g and ~138 m²/g) and wide Eg (3.14 eV and 3.19 eV). This outcome is in agreement with references supporting the superior role of the charge separation by the graphene compared to the increase of SSA of the photocatalyst [16,43], as well as to the narrowing of the Eg which is widely accepted as a major parameter for enhancing visible light activity.

The above findings also indicate that there is a difference in the interaction between the TiO₂ nanoparticles and the graphene sheets depending on the type of graphene used for preparation of composite photocatalysts. In general, for titania/graphene composites it has been widely recognized that the photogenerated electrons from the TiO₂ component are easily transferred to graphene sheets [71]. These electrons may be involved in reduction reactions e.g. CO₂ conversion to hydrocarbons [43] or formation of active O₂^{•−} species with the oxygen from the environment. Most importantly, their removal from the titania results in decrease of the recombination of electron-hole pairs on the surface of TiO₂. This phenomenon known as electron trapping, directly increases the efficiency of the photocatalyst by increasing the lifetime of the holes favoring thus the formation of highly oxidative OH[•], HO₂[•] radicals [37]. Taking into account that the NOx oxidation mechanism is governed mainly by the OH[•], HO₂[•] species [72,73], increased activity of graphene/TiO₂ photocatalysts can be expected. For the TiO₂/G samples however, the expected increased efficiency in NOx oxidation was not observed especially when UV light was applied.

The differences in the photocatalytic behavior of TiO₂/G and TiO₂/rGO materials can be linked to differences in the band gap of the two types of graphene ssG and rGO. The single- and few-layer graphene without oxygen content has zero band gap with limited tuning capabilities [74]. In contrast, the band gap of rGO is non-zero and depends on the oxygen content varying between 3.5 eV and 1 eV in parallel with the increase of the C/O ratio [75,76]. At the TiO₂/graphene interface, when photogenerated electrons are transferred to graphene sheets, they are more likely to recombine at the valence band of TiO₂ nanoparticles in the case of ssG than in the case of rGO, which presumably has a non-zero band gap. Thus, the recorded low efficiency under UV light of the TiO₂/G can be explained by the electron-hole recombination. Also, the beneficial role of the highly conductive pure graphene might have been hindered in our experiment by the presence of residual surfactant Pluronic F127. The recorded better performance of the TiO₂/rGO under visible light is in accordance with results reported in references [14,16,27] which was accredited to the coupling of the conductive and valence band levels of the TiO₂ and rGO semiconductors. The decrease in efficiency for higher graphene loadings was associated with the shielding effect restricting the TiO₂ nanoparticles from absorbing UV and visible light [77].

Importantly, the two types of composite photocatalysts TiO₂/G and TiO₂/rGO exhibited extremely low NO₂ emission which decreased with the increase of the graphene content. Due to affinity of graphene materials to NO₂ gas, this intermediate product remains adsorbed on the surface of the photocatalyst until part of it or the whole amount is oxidized to solid HNO₃. This leads to the measured low NO₂ concentrations. Our experimental results are in consistence with the theoretically estimated favorable NO₂ adsorption on graphene through an interaction between the NO₂ molecules and the π -conjugated system in graphene sheets [78].

Finally, the benefits of the present work can be summarized as: (a) manufacture of TiO₂/G nanocomposites through in situ synthesis of TiO₂ in hydrophilic non-oxidized graphene dispersions; (b) comparative examination of two types of graphene i.e., reduced GO and pure graphene G for coupling with TiO₂ and photocatalytic NOx oxidation.

4. Conclusions

Nanocomposite TiO₂/graphene powders with different graphene loading were prepared via in situ synthesis of anatase TiO₂ in presence of surfactant-stabilized graphene (ssG) and graphene oxide (GO) at solvothermal conditions.

According to the XRD results, the addition of graphene did not influence the crystallinity of the photocatalysts. The average crystallite size of the TiO_2 and $\text{TiO}_2/\text{graphene}$ composite materials ranged between 5 and 10 nm. Diffraction peaks originating from the graphene component were not recorded indicating the formation of well-mixed and uniform $\text{TiO}_2/\text{graphene}$ nanocomposites. Reduction of GO to rGO occurred during the synthesis.

SEM and FT-IR analysis confirmed the exfoliation of the graphite and the graphite oxide, while the presence of graphene component in the composite materials was not observed due to the low loading. Its incorporation in the composites with the highest (1%) loading was demonstrated by the Raman measurements and TEM study.

The porosity was influenced by the addition of both surfactant (Pluronic F127) and graphene (ssG and GO). The highest SSA values were measured for the pure titania and the composites with largest graphene content.

The band gap energy was not altered by the surfactant, while the increase of the graphene content resulted in narrowing of E_g .

The photocatalytic performance of the composites in NO_x removal displayed two trends. First, the efficiency of the composite photocatalysts was slightly improved under UV light in both (ssG- and rGO-containing TiO_2) cases reaching a maximum efficiency at low ssG and rGO loadings. The enhancement was attributed to the interaction between TiO_2 nanoparticles and graphene sheets, with the latter acting as electron traps in the case of ssG and photosensitizer in the case of rGO. The enhancement was more prominent under visible light where the rGO is activated. Second, the composite photocatalysts exhibited low NO_2 release with the addition of ssG and rGO, which was related to affinity of NO_2 molecules to graphene sheets. The De- NO_x efficiency of TiO_2/rGO photocatalysts was significantly increased which renders such materials promising photocatalysts for NO_x removal from ambient air.

Acknowledgements

The financial support from FP7 project AUTOSUPERCAP and GSRT projects 12CN205- PhotoTiGRA and GE-1813-PolyGRAPH is highly appreciated.

References

- [1] M.L. Bell, D.L. Davis, T. Fletcher, *Environ. Health Perspect.* 112 (2004) 6–8.
- [2] D. Davis, *When Smoke Ran like Water: Tales of Environmental Deception and the Battle against Pollution*, reprint edition, Basic Books, 2003.
- [3] R. Guicherit, D. van den Hout, *Air Pollution by Nitrogen Oxides*, in: L. Grant, T. Schneider (Eds.), Elsevier Scientific Publishing Company, 1982, pp. 15–30.
- [4] J.S. Levine, T.R. Augustsson, I.C. Andersont, J.M. Hoell, D.A. Brewer, *Atmos. Environ.* 18 (1984) 1797–1804.
- [5] B. Son, W. Yang, P. Breyse, T. Ching, Y. Lee, *Environ. Res.* 94 (2004) 291–296.
- [6] A. Fujishima, K. Honda, *Nature* 238 (1972) 37–38.
- [7] A.L. Linsebigler, G. Lu, J.T. Yates, *Chem. Rev.* 95 (1995) 735–758.
- [8] K. Hashimoto, H. Irie, A. Fujishima, *Jpn. J. Appl. Phys.* 44 (2005) 8269–8285.
- [9] R. Thiruvengadachari, S. Vigneswaran, I.S. Moon, *Kor. J. Chem. Eng.* 25 (2008) 64–72.
- [10] S. Malato, P. Fernandez-Ibanez, M.I. Maldonado, J. Blanco, W. Gernjak, *Catal. Today* 147 (2009) 1–59.
- [11] R. Leary, A. Westwood, *Carbon* 49 (2011) 741–772.
- [12] K.S. Novoselov, A.K. Geim, S.V. Morozov, D. Jiang, Y. Zhang, S.V. Dubonos, I.V. Grigorieva, A.A. Firsov, *Science* 22 (2004) 666–669.
- [13] Q. Xiang, J. Yu, M. Jaroniec, *Chem. Soc. Rev.* 41 (2012) 782–796.
- [14] C. Han, M.Q. Yang, B. Weng, Y.J. Xu, *Phys. Chem. Chem. Phys.* 16 (2014) 16891–16903.
- [15] N. Zhang, M.Q. Yang, Z.R. Tang, Y.J. Xu, *ACS Nano* 8 (2014) 623–633.
- [16] Y. Zhang, Z.R. Tang, X. Fu, Y.J. Xu, *ACS Nano* 5 (2011) 7426–7435.
- [17] N. Zhang, Y. Zhang, Y.J. Xu, *Nanoscale* 4 (2012) 5792–5813.
- [18] Y. Zhang, N. Zhang, Z.R. Tang, Y.J. Xu, *Phys. Chem. Chem. Phys.* 14 (2012) 9167–9175.
- [19] M.Q. Yang, Y.J. Xu, *Phys. Chem. Chem. Phys.* 15 (2013) 19102–19118.
- [20] Y. Zhang, Z.R. Tang, X. Fu, Y.J. Xu, *ACS Nano* 4 (2010) 7303–7311.
- [21] V. Nicolosi, M. Chhowalla, M.G. Kanatzidis, M.S. Strano, J.N. Coleman, *Science* 340 (2013) 1226419.
- [22] W. Park, J. Hu, L.A. Jauregui, X. Ruan, Y.P. Chen, *Appl. Phys. Lett.* 104 (2014) 113101.
- [23] K.P. Loh, Q. Bao, G. Eda, M. Chhowalla, *Nat. Chem.* 2 (2010) 1015–1024.
- [24] M.Q. Yang, N. Zhang, M. Pagliaro, Y.J. Xu, *Chem. Soc. Rev.* 43 (2014) 8240–8254.
- [25] C. Chen, W. Cai, M. Long, B. Zhou, Y. Wu, D. Wu, Y. Feng, *ACS Nano* 4 (2010) 6425–6432.
- [26] G. Jiang, Z. Lin, C. Chen, L. Zhu, Q. Chang, N. Wang, W. Wei, H. Tang, *Carbon* 49 (2011) 2693–2701.
- [27] T.D.N. Phan, V.H. Pham, E.W. Shin, H.D. Pham, S. Kim, J.S. Chung, E.J. Kim, S.H. Hur, *Chem. Eng. J.* 170 (2011) 226–232.
- [28] J.C. Liu, H.W. Bai, Y.J. Wang, Z.Y. Liu, X.W. Zhang, D.D. Sun, *Adv. Funct. Mater.* 20 (2010) 4175.
- [29] Y. Park, S.H. Kang, W. Choi, *Phys. Chem. Chem. Phys.* 13 (2011) 9425–9431.
- [30] P. Wang, J. Wang, X. Wang, H. Yu, Jianguo Yu, M. Lei, Y. Wang, *Appl. Catal. B – Environ.* 132–133 (2013) 452–459.
- [31] K. Li, J. Xiong, T. Chen, L. Yan, Y. Dai, D. Song, Y. Lv, Z. Zeng, *J. Hazard. Mater.* 250–251 (2013) 19–28.
- [32] Y. Li, J. Yan, Q. Su, E. Xie, W. Lan, *Mater. Sci. Semicond. Process.* 27 (2014) 695–701.
- [33] X. Pan, Y. Zhao, S. Liu, C.L. Korzeniewski, S. Wang, Z. Fan, *ACS Appl. Mater. Interfaces* 4 (2012) 3944–3950.
- [34] J.S. Lee, K.H. You, C.B. Park, *Adv. Mater.* 24 (2012) 1084–1088.
- [35] Y. Zhang, C. Pan, *J. Mater. Sci.* 46 (2011) 2622–2626.
- [36] H. Zhang, P. Xu, G. Du, Z. Chen, K. Oh, D. Pan, Z. Jiao, *Nano Res.* 4 (2011) 274–283.
- [37] S.D. Perera, R.G. Mariano, K. Vu, N. Nour, O. Seitz, Y. Chabal, K.J. Balkus, *ACS Catal.* 2 (2012) 949–956.
- [38] Y.H. Ng, I.V. Lightcap, K. Goodwin, M. Matsumura, P.V. Kamat, *J. Phys. Chem. Lett.* 1 (2010) 2222–2227.
- [39] P. Fernandez-Ibanez, M.I. Polo-Lopez, S. Malato, S. Wadhwa, J.W.J. Hamilton, P.S.M. Dunlop, R. D'Sa, E. Magee, K. O'Shea, D.D. Dionysiou, J.A. Byrne, *Chem. Eng. J.* 261 (2015) 36–44.
- [40] W. Fan, Q. Lai, Q. Zhang, Y. Wang, *J. Phys. Chem. C* 115 (2011) 10694–10701.
- [41] X. An, J.C. Yu, *RSC Adv.* 1 (2011) 1426–1434.
- [42] H.G. Lee, G.S. Anand, S. Komathi, A.I. Gopalan, S.W. Kang, K.P. Lee, *J. Hazard. Mater.* 283 (2015) 400–409.
- [43] Y.T. Liang, B.K. Vijayan, K.A. Gray, M.C. Hersam, *Nano Lett.* 11 (2011) 2865–2870.
- [44] L. Guardia, M.J. Fernandez-Merino, J.I. Paredes, P. Solis-Fernandez, S. Villar-Rodil, A. Martinez-Alonso, J.M.D. Tascon, *Carbon* 49 (2011) 1653–1662.
- [45] W.S. Hummers, R.E. Offeman, *J. Am. Chem. Soc.* 80 (1958) 1339.
- [46] B. Mahltig, E. Gutmann, D.C. Meyer, *Mater. Chem. Phys.* 127 (2011) 285–291.
- [47] ISO/DIS 22197-1, 2007, pp. 1–11.
- [48] N. Todorova, T. Giannakopoulou, S. Karapati, D. Petridis, T. Vaimakis, C. Trapalis, *Appl. Surf. Sci.* 319 (2014) 113–120.
- [49] T. Giannakopoulou, N. Todorova, G. Romanos, T. Vaimakis, R. Dillert, D. Bahnemann, C. Trapalis, *Mater. Sci. Eng. B* 117 (2012) 1046–1052.
- [50] M. Shi-Jia, S. Yu-Chang, X. Li-Hua, L. Si-Dong, H. Te, T. Hong-Bo, *Chin. Phys. Lett.* 30 (2013) 096101.
- [51] D.A. Dikin, S. Stankovich, E.J. Zimney, R.D. Piner, G.H.B. Dommett, G. Evmenenko, S.T. Nguyen, R.S. Ruoff, *Nature* 448 (2007) 457–460.
- [52] D.D. Dunuila, C.D. Gagliardi, K.A. Berglund, *Chem. Mater.* 6 (1994) 1556–1562.
- [53] S. Das, M. Bhunia, A. Bhaumik, *Dalton Trans.* 39 (2010) 4382–4390.
- [54] F. Bonaccorso, Z. Sun, T. Hasan, A.C. Ferrari, *Nat. Photonics* 4 (2010) 611–622.
- [55] M. Lotya, Y. Hernandez, P.J. King, R.J. Smith, V. Nicolosi, L.S. Karlsson, F.M. Blighe, S. De, Z. Wang, I.T. McGovern, G.S. Duesberg, J.N. Coleman, *J. Am. Chem. Soc.* 131 (2009) 3611–3620.
- [56] S. Xu, L. Yong, P. Wu, *ACS Appl. Mater. Interfaces* 5 (2013) 654–662.
- [57] D. Li, M.B. Muller, S. Gilje, R.B. Kaner, G.G. Wallace, *Nat. Nanotechnol.* 3 (2008) 101–105.
- [58] S.T. Sun, P.Y. Wu, *Phys. Chem. Chem. Phys.* 13 (2011) 21116–21120.
- [59] J. Shen, T. Li, Y. Long, M. Shi, N. Li, M. Ye, *Carbon* 50 (2012) 2134–2140.
- [60] J. Coates, *Encyclopedia of Analytical Chemistry*, in: R.A. Meyers (Ed.), John Wiley & Sons Ltd, 2000, pp. 10815–10837.
- [61] J.G. Yu, H.G. Yu, B. Cheng, X.J. Zhao, J.C. Yu, W.K. Ho, *J. Phys. Chem. B* 107 (2003) 13871–13879.
- [62] K.N. Kudin, B. Ozbas, H.C. Schniepp, R.K. Prud'homme, I.A. Aksay, R. Car, *Nano Lett.* 8 (2008) 36–41.
- [63] A.C. Ferrari, J.C. Meyer, V. Scardaci, C. Casiraghi, M. Lazzeri, F. Mauri, S. Piscanec, D. Jiang, K.S. Novoselov, S. Roth, A.K. Geim, *Phys. Rev. Lett.* 97 (2006) 187401.
- [64] D. Yang, A. Velamakanni, G. Bozkou, S. Park, M. Stoller, R.D. Piner, S. Stankovich, I. Jung, D.A. Field, C.A. Ventrice, R.S. Ruoff, *Carbon* 47 (2009) 145–152.
- [65] T. Ohsaka, F. Izumi, Y. Fujiki, *J. Raman Spectrosc.* 6 (1978) 321–324.
- [66] W.F. Zhang, Y.L. He, M.S. Zhang, Z. Yin, Q. Chen, *J. Phys. D: Appl. Phys.* 33 (2000) 912–916.
- [67] P. Kubelka, F. Munk, *Z. Tekn. Phys.* 12 (1931) 593.
- [68] P. Kubelka, *J. Opt. Soc. Am.* 38 (1948) 448.
- [69] A.B. Murphy, *Sol. Energy Mater. Sol. Cells* 91 (2007) 1326–1337.
- [70] H. Mahmood, A. Habib, M. Mujahid, M. Tanveer, S. Javed, A. Jamil, *Mater. Sci. Semicond. Process.* 24 (2014) 193–199.
- [71] R. Sellappan, J. Sun, A. Galeckas, N. Lindvall, A. Yurgens, A. Yu Kuznetsov, D. Chakarov, *Phys. Chem. Chem. Phys.* 15 (2013) 15528–15537.
- [72] R. Dillert, A. Engel, J. Grobe, P. Lindner, D.W. Bahnemann, *Phys. Chem. Chem. Phys.* 15 (2013) 20786–20886.

- [73] Y. Ohko, Y. Nakamura, N. Negishi, S. Matsuzawa, K. Takeuchi, J. Photochem. Photobiol. 205 (2009) 28–33.
- [74] Y. Zhang, T.T. Tang, C. Girit, Z. Hao, M.C. Martin, A. Zettl, M.F. Crommie, Y.R. Shen, F. Wang, Nature 459 (2009) 820–823.
- [75] A. Mathkar, D. Tozier, P. Cox, P. Ong, C. Galande, K. Balakrishnan, A.L.M. Reddy, P.M. Ajayan, J. Phys. Chem. Lett. 3 (2012) 986–991.
- [76] M. Acik, Y.J. Chabal, J. Mater. Sci. Res. 2 (2013) 101–112.
- [77] K.F. Mak, M.Y. Sfeir, Y. Wu, C.H. Lui, J.A. Misewich, T.F. Heinz, Phys. Rev. Lett. 101 (2008) 196405.
- [78] O. Leenaerts, B. Partoens, F.M. Peeters, Phys. Rev. B 77 (2008) 1–6.